Microfluid Nanofluid (2011) 10:563–577
DOI 10.1007/s10404-010-0690-4

RESEARCH PAPER

Local heat transfer process and pressure drop in a micro-channel integrated with arrays of temperature and pressure sensors

H. S. Ko · C. Gau

Received: 19 July 2010 / Accepted: 6 September 2010 / Published online: 21 October 2010

Abstract One of the most important components in micro-fluidic system is the micro-channel which involves complicated flow and transport process. This study presents micro-scale thermal fluid transport process inside a micro-channel with a height of 37 μm. The channel can be heated on the bottom wall and is integrated with arrays of pressure and temperature sensors which can be used to measure and determine the local heat transfer and pressure drop. A more simplified model with modification of Young's Modulus from the experimental test is used to design and fabricate the arrays of pressure sensors. Both the pressure sensors and the channel wall use polymer materials which greatly simplify the fabrication process. In addition, the polymer materials have a very low thermal conductivity which significantly reduces the heat loss from the channel to the ambient that the local heat transfer can be accurately measured. The air flow in the micro-channel can readily become compressible even at a very low Reynolds number condition. Therefore, simultaneous measurement of both the local pressure drop and the temperature on the heated wall is required to determine the local heat transfer. Comparison of the local heat transfer for a compressible air flow in micro-channel is made with the theoretical prediction based on incompressible air flow in large-scale channel. The comparison has clarified many of the conflicting results among different works.

Keywords Micro-scale heat transfer · Micro-channel · Pressure sensor arrays · Temperature sensor arrays

H. S. Ko · C. Gau (✉)
Institute of Aeronautics and Astronautics and Center for Micro/Nano Science and Technology, National Cheng Kung University, Tainan 70101, Taiwan
e-mail: gauc@mail.ncku.edu.tw

List of symbols

A	Cross section area of the channel
b	Width of the diaphragm
c_p	Specific heat of air
D_h	Hydraulic diameter, 2H
e	Enthalpy
E	Young's modulus
Gz	Graetz number defined by Eq. 29
H	Channel height
h_o	Convective heat transfer coefficient based on the flow temperature at the inlet
h_b	Convective heat transfer coefficient based on the bulk temperature of the flow
k	Specific heat ratio, c_p/c_v
K	Thermal conductivity of air
$\dot{m}$	Mass flow rate of the air in the channel
Nu	Nusselt number defined by Eq. 21
p	Pressure
Pr	Prandtl number, v/α
$\dot{q}$	Heat transfer rate
$\dot{q}_w$	The heat flux imposed along the bottom wall by the electric heaters
Re	Reynolds number, UD_h/υ
t	Thickness of the diaphragm
T	Temperature
U	Mean flow velocity in the channel
u	Streamwise velocity
v	Velocity in the y-axis
w	Channel width
x	Streamwise distance from the entrance of the channel
y	Normal distance from the heated wall
α	Thermal diffusivity of air
β	Poisson's ratio
δ	Deformation of the diaphragm
ε	Strain in the diaphragm

v Kinematic viscosity of air
ρ Density of air

Subscripts
b Bulk
i Inlet
o Outlet
w Wall
x A streamwise location from the entrance of the channel

1 Introduction

Understanding of the local micro-scale flow and heat transfer process is very important not only for basic research but also for practical applications in lab-on-chip or MEMS thermal systems (Craighead 2006; Li 2004). The lab-on-chip system has seen the rapid development of new methods of fabrication, and of the components—the micro-channels that serve as pipes, and other structures that form valves, mixers, and pumps—that are essential elements of micro-chemical "factories" on a chip. Therefore, many of the micro-channels are used to transport fluids for chemical or biological processing. Specially designed channel is used for mixing of different fluids or separating different species. It appears that mass or momentum transport process inside the channel is very important. In fact, the transfer process of the mass is very similar to the transfer process of the heat due to similarity of the governing equations for the mass and the heat (Incropera et al. 2007). It can be readily derived that the Nusselt number divided by the Prandtl number to the nth power is equal to the Sherdwood number (defined as the convective mass transfer coefficient times the characteristic length and divided by the diffusivity of the mass) divided by the Schmidt number (defined as the kinematic viscosity divided by the diffusivity of the mass) to the nth power. Understanding of the heat transfer can help to understand the mass transfer or even the momentum transfer inside the micro-channel (Incropera et al. 2007).

On the other hand, the need for a greater cooling capacity in computer's CPU chip has pushed a move toward possibility of using micro-channel cooling techniques. Micro-channel cooling techniques have been shown to remove large amount of heat and has the very high potential to solve today's or tomorrow's high power density CPU chip (Prasher et al. 2005; Tuckerman and Pease 1981). However, basic understanding of the micro-scale heat transfer process and acquisition for an accurate heat transfer data in the micro-channel is still not possible today. This heavily relies on the successful fabrication of a complicated micro-channel system integrated with dedicated sensors. Numerical calculation using some commercial codes, such COMSOL or FLUENT, may be utilized conveniently to study micro-scale flow and heat transfer in the micro-channel. However, these numerical schemes does not account for the micro-scale effects, such as the slip flow condition on the wall, the electric double layer occurred for liquid flow along the wall of the micro-channel. In addition, the numerical results may not be reliable without confirmation by the experimental data.

Unfortunately, most of the current micro-channels used or fabricated could not provide local heat transfer and pressure drop information due to difficulty in incorporating both the micro-sensors and the micro-heaters into the micro-channel in accurate locations for flow and heat transfer measurements, or the improper control of the heat loss. The channels fabricated by Jiang et al. (1999) will lead to a large amount of conduction in the streamwise direction; therefore, local heat transfer data could not be obtained. Good review articles on flow and heat transfer study in micro-channel are available (Morini 2004; Rostami et al. 2002; Natrajan and Christensen 2010; Dongari et al. 2009). All the heat transfer data reported is an average of heat transfer over the entire micro-channel. That is, by measuring the bulk flow temperature at the inlet and the outlet of the channel, the average heat transfer for this channel can be obtained. No temperature sensors can be inserted into the channel to acquire the local heat transfer data. Ko et al. (2007b) appear to be the first work to obtain the local heat transfer in a heated micro-channel integrated with array of micro-sensors for temperature measurements. Using polymer material, which has a very low thermal conductivity, to fabricate a channel and reduce the heat loss to the ambient, very accurate measurements on the heat transfer coefficient has been obtained. However, the heat transfer data measured do not account for the compressibility of the flow. Very peculiar heat transfer data, which is significantly different from the ones measured in large-scale channel, is found. Later, it has been found in a micro-channel fabricated (Ko et al. 2008), which is integrated with arrays of pressure sensors that the air flow is very compressible even at a very low Reynolds number condition. Therefore, accurate measurements of the heat transfer in a micro-channel could not be obtained without accounting for the compressible effect of the flow. This requires simultaneous measurements of both the local temperature distribution along the heated wall and the local pressure distribution along the channel. Therefore, array of both micro-temperature and micro-pressure sensors are required to be integrated along the channel system to obtain local heat transfer in a micro-channel flow. The local heat transfer is important not only in the micro-thermal transport process, but also in the micro-mass transport process

which may be frequently encountered in a lab-on-chip system.

Due to the difficulty in incorporating arrays of micro-sensors for pressure measurements in a micro-channel to obtain local pressure drop or friction factor information, most of the pressure drop or friction factor measured are based on the pressures at the inlet and the outlet of the channel. This leads to many of the data conflicting to each other (Bayraktar and Pidugu 2006; Rostami et al. 2002; Koo and Kleinstreuer 2003) due to uncertainty in estimation of the entry length and the pressure loss at the entrance or the outlet. There are a few works (Zohar et al. 2002; Lee et al. 2002) which fabricate a complicated channel system integrated with arrays of micro-pressure sensors to obtain pressure drop inside the channel. However, fabrication of this channel is limited to a height of 1.2 μm. Since the substrate used is silicon, surface micro-machining process is used to fabricate both the channel and the arrays of the pressure sensors. The fabrication processes developed previously were very complex and could not be used in polymer material or plastics. To simplify the fabrication process, polymer material is suggested to use.

It appears that it is required to develop pressure sensors which can be integrated with channel system using polymer materials as proposed in this study. Fabrication of this complicated system can be greatly simplified using polymer material. The miniaturized pressure sensors developed by Ko et al. (2007a) employ SU-8 material, which can be readily integrated with a micro-channel for pressure measurements (Ko et al. 2008). However, the design procedure is rather complicated. Here a more simplified model, with modification of the Young's Modulus from the experimental data, is used to design and fabricate arrays of polymer micro-pressure sensors which can be readily integrated with the current channel system.

The MEMS technique is adopted here to fabricate a micro-channel with the height of 37 μm. In fact, the channel can be fabricated at any desired thickness and can be integrated with two arrays pressure sensors, as shown in Fig. 1. The channel can be made strong enough to withhold high-pressure gas flow. The wall surface can be made smooth enough to eliminate wall roughness effect. Measurements of local pressures along the channel can be made by the flow which can enter through the small tunnels into the cavities of the pressure sensors and push the diaphragm of each cavity. The deflection of the diaphragm can be measured by the sensor material deposited on top of each cavity. The greater advantages of the fabrication process for this sensor is that large amount of sensors can be made together with other micro-system, such as a micro-channel, to study or measure pressure information in various regions of the micro-system.

In addition, this channel can be integrated with micro-heaters on the wall to provide uniform heating, and an array of miniaturized temperature sensors, as shown in Fig. 1, to provide measurements of local temperatures on the wall. Therefore, the channel can provide simultaneous measurements of both the temperature on the heated wall and the pressure drop along the channel. The compressibility effect of the gas flow can be taken into account so that accurate heat transfer data can be obtained. This requires an analytical result for the pressure drop relation with the density or the mass flow rate for the case when the heat transfer occurs. In this article, however, a simplified theoretical analysis for the pressure drop variation with the mass flow rate inside the channel for the case without heat transfer is carried out first, which can be validated by comparison with the data measured in the current channel. By fitting with the pressure drop data for the case when the heat transfer occurs, this theoretical analysis for the pressure drop variation with the mass flow rate or the density can be modified and used for the case when the heat transfer occurs. More detailed analyses and discussion are provided. Special features of the detailed thermal and flow characteristics inside the micro-channel are presented for the first time in the literature.

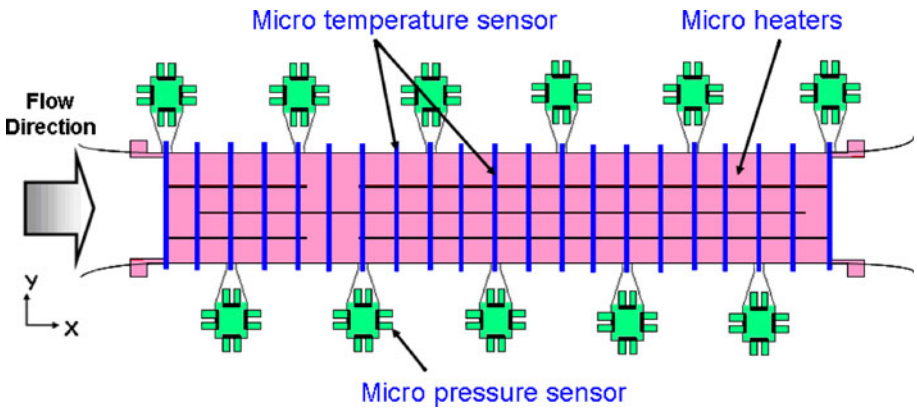

Fig. 1 Micro-channel system with arrangements of arrays of miniaturized pressure sensors, miniaturized temperature sensors, and two sets of heaters used for study of micro-scale heat transfer and pressure drop of air flow

2 Theory

2.1 Analytical model for design of miniaturized pressure sensor

A simplified analytical analysis can provide proper design of the diaphragm before fabrication, such as the size of the SU-8 diaphragm which is determined from the pressure range covered in the experiments, the maximum strain that the diaphragm can sustain, and the sensitivity required. Therefore, the theoretical analysis together with experiments of diaphragm deformation at different applied pressures is performed for design of the SU-8 diaphragm. The deformation of SU-8 diaphragm can be modeled as a square shell or plate with four edge clamped under a uniform normal pressure force. The maximum deflection of the diaphragm can be found from the approximated solution of the deformation as follows (Boresi et al. 1993):

$$\delta_{\max} = C\left(1-\beta^2\right)\frac{pb^4}{Et^3} \tag{1}$$

where C is $\frac{0.032}{1+a^4}$, with the assumption that all edges of the plate are clamped, and a is ratio of the width to the length of the plate. However, C obtained by Guckel et al. (1990) is 0.0152. The maximum strain of the SU-8 diaphragm is (Boresi et al. 1993):

$$\varepsilon_{\max} = 0.308\left(1-\beta^2\right)\frac{pb^2}{Et^2}. \tag{2}$$

In order to confirm the predictions from the analysis, experiments for diaphragm deformation of the SU-8 material have been performed, as shown in Fig. 2. The diaphragm is spin-coated on a (100) silicon substrate which is pre-deposited with silicon nitride. The silicon nitride is patterned to define the size of cavity which is then etched by the KOH. The entire silicon substrate is pressed into a cavity made of a Plexiglas chunk which is connected with pipe line supplying gas at desired pressures. A profilometer is used to measure the deformation of diaphragm under different gas pressures. The entire fabrication for the diaphragm test experiments is described in the following:

(1) A low stress nitride is deposited on the both side of silicon wafer by PECVD, as shown in Fig. 3a. It can be used as both the protection mask and the etch stop during the later long period of wet etch process to form the cavity.
(2) The low stress nitride on the bottom of the substrate is patterned, as shown in Fig. 3b, to allow etch of the cavity by the KOH, and the patterned size required can be calculated from the wafer thickness and the size of cavity required for diaphragm deformation. The side walls of the cavity should be the (111) planes having a inclination of 54.7° from the horizontal (100) plane.
(3) A 10-μm thick SU-8 film is spin-coated on the top of the silicon substrate. Then, soft bake, exposure, and post-exposure bake are used to form the solidified film of SU-8.
(4) To open a cavity for diaphragm movement the KOH solution with very high etching selectivity of silicon versus silicon nitride is used. The wet etch process is at 90°C for 5–6 h until silicon in the cavity is completely removed, as shown in Fig. 3c.
(5) Finally, the etch stop of nitride film under the SU-8 film is removed by the RIE dry etch, as shown in Fig. 3d.

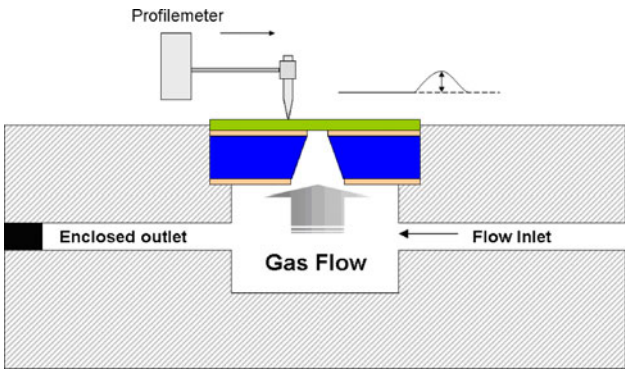

Fig. 2 Diaphragm deflection measurements

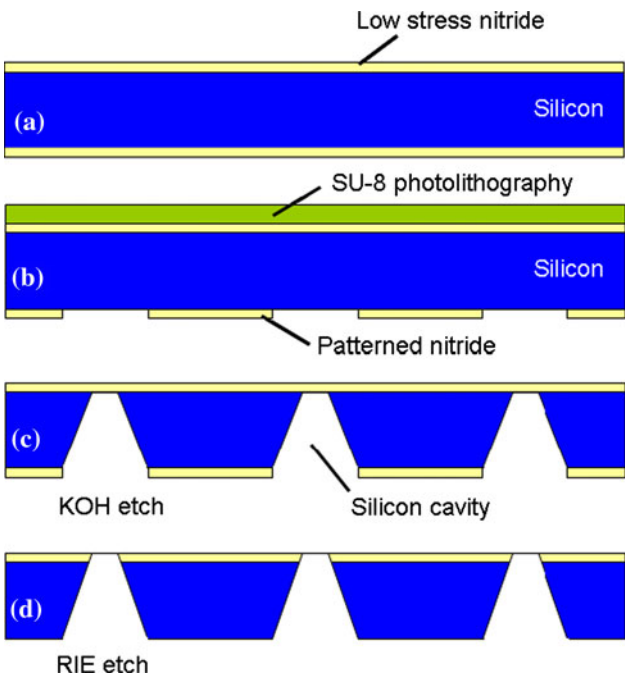

Fig. 3 Fabrication processes of the SU-8 diaphragm, which is used for deflection testing

The completed diaphragm test chip is mounted on a PMMA, as shown in Fig. 4a. The diaphragm has a thickness of 9.7 μm with 193-μm wide square. The applied gas pressure varies from 0 to 276 kPa (0–40 Psig). The deformation variation of the diaphragm with the pressures is measured, as shown in Fig. 4b. The maximum deformation at a given pressure can be compared with the prediction from Eq. 1. To use Eq. 1, however, both the Poisson ratio and the Young's Modulus of the materials have to be determined. The Poisson ratio reported by Dellmann et al. (1997) has a small variation (0.22–0.24) which has a negligible effect on the maximum deflection; while the Young's Modulus of the SU-8 varies significantly depending very much on the light exposure, the heating and cooling conditions (Lorenz et al. 1997; Dellmann et al. 1997). Therefore, the Young's Modulus of the current SU-8 diaphragm made by the above process is measured by a nanoindenter (MTS Nano Indenter XP, USA). An average of Young's Modulus at five points is obtained, which is 0.48 MPa and is used for the calculation. The maximum deformation calculated by Eq. 1 is compared with the data, as shown in Fig. 4c. It appears that the data has a good agreement with the prediction, but with a small deviation of about 10%. The deviation may be caused by the non-uniformity of the diaphragm during the spin coat process, and or the measurement error from the Young's Modulus which is obtained from measurements of the nanoindenter at five different locations. Therefore, the experimental data is fitted with Eq. 1 by adjusting the Young's Modulus of the SU-8. A good fit of the data can be obtained when the Young's Modulus of the SU-8 is 5 MPa, as shown by the dash line in Fig. 4c.

With correct Young's Modulus of the SU-8, the maximum deflection can be accurately predicted by Eq. 1. Therefore, Eq. 2 is used to find the maximum strain that occurs in the SU-8 diaphragm. Since the maximum strain that the SU-8 can endure is 0.77% (Guckel 1990), the thickness and the size of the diaphragm can be estimated and designed by Eq. 2 with correct Poisson ratio and Young's Modulus of the material. For a pressure range from 0 to 413 kPa, the diaphragm designed for each of the pressure sensors has the size of $150 \times 150\ \mu m^2$ and a thickness of approximately 9 μm.

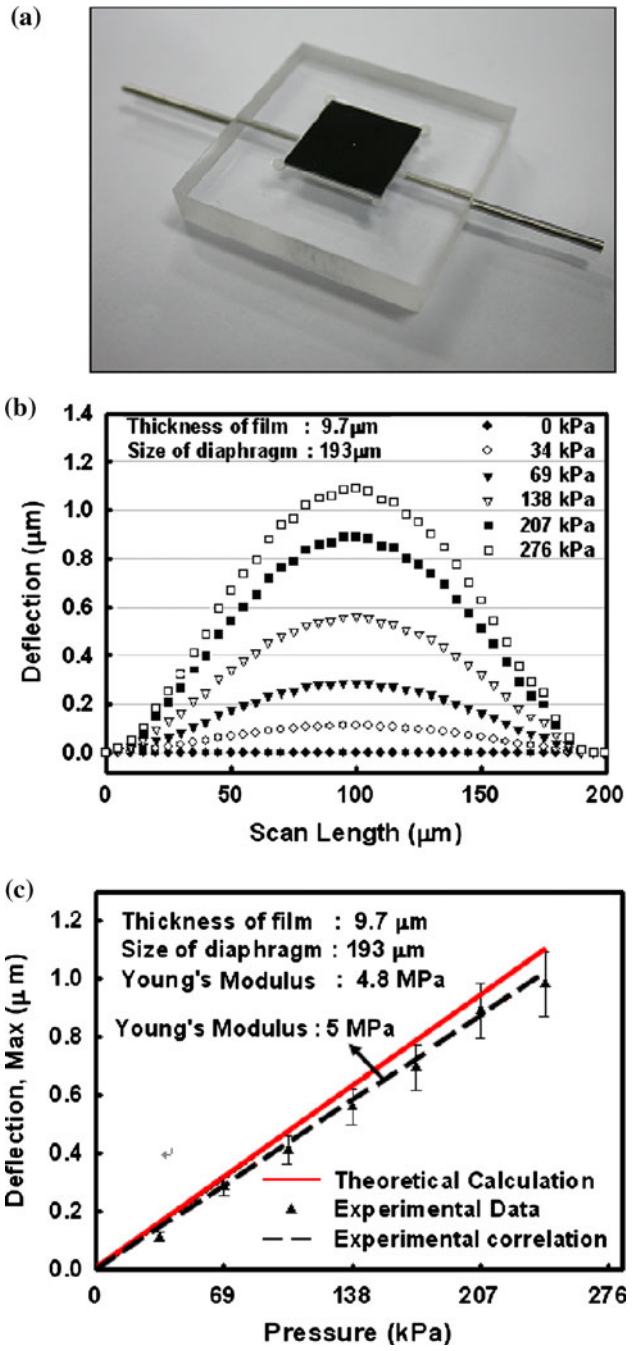

Fig. 4 The deflection testing of SU-8 diaphragm: **a** completed testing model, **b** measured diaphragm deflection profile, and **c** comparison of the maximum deflection between the prediction and the experimental data

2.2 Analysis of the pressure drop

To understand the characteristics of the micro-flow inside a micro-channel, theoretical analysis of the micro-flow inside the channel without occurrence of heat transfer is performed first. The analysis is used to compare with the experimental data in Sect. 5.1. Since the channel has a large width (500 μm) in comparison with its height (37 μm), the channel flow in this study can be assumed as a steady, 2D, laminar flow between two parallel plates. The configuration with the coordinate system and flow velocity of micro-channel flow are shown in Fig. 1. Therefore, the governing equations of the flow in this micro-channel system can be written as follows (Incropera et al. 2007):

Continuity:

$$\frac{\partial \rho u}{\partial x}+\frac{\partial \rho v}{\partial y}=0 \tag{3}$$

Momentum:

$$\rho\left(u\frac{\partial u}{\partial x}+v\frac{\partial u}{\partial y}\right)=-\frac{\partial p}{\partial x}+\mu\left(\frac{\partial^2 u}{\partial x^2}+\frac{\partial^2 u}{\partial^2 y}\right) \tag{4}$$

$$\rho\left(u\frac{\partial v}{\partial x}+v\frac{\partial v}{\partial y}\right)=-\frac{\partial p}{\partial y}+\mu\left(\frac{\partial^2 v}{\partial x^2}+\frac{\partial^2 v}{\partial y^2}\right). \tag{5}$$

The micro-channel is actually fabricated by very low thermal conductivity materials, which can be considered as a well-insulated channel. Therefore, without heating on the wall the gas flow inside the channel can be assumed to be undergoing isentropic process as follows:

$$\frac{p}{\rho^k}=\text{const.} \tag{6}$$

If non-slip boundary condition on the wall is used, then the boundary condition can be written as:

$$U(y)_{\mathrm{w}}=0 \tag{7}$$

In Eq. 6, k is the ratio of specific heat c_p versus c_v. For micro-flow in parallel plate channel, the height is much smaller than the width of the channel. One can assume that not only the streamwise velocity is much greater than the transverse velocity, but also the gradient normal to the surface of channel in the momentum equations is much larger than along the channel as follows:

$$u \gg v, \quad \frac{\partial}{\partial y} \gg \frac{\partial}{\partial x}, \quad \text{and} \quad \frac{\partial^2 u}{\partial y^2} \gg \frac{\partial^2 u}{\partial x^2} \tag{8}$$

Therefore, the momentum equations for the micro-channel flow can be simplified as

$$\frac{\partial p}{\partial x}=\mu\frac{\partial^2 u}{\partial y^2} \tag{9}$$

$$\frac{\partial p}{\partial y}=0 \tag{10}$$

Equations 9 and 10 mean that the pressure varies only in the streamwise direction. Therefore, Eq. 9 can be readily solved analytically. This equation is the same as the one for channel flow in the fully developed region. The pressure distribution measurements presented in the later section indicate that the entry length of the flow in the micro-channel could hardly be observed. It means that the flow in most part of the micro-channel is fully developed except in the very short entry region where x is not large as compared with the width of the channel. The solution of Eq. 9 is a parabolic velocity profile as follows:

$$u(y)=\frac{y^2}{2\mu}\frac{\mathrm{d}p}{\mathrm{d}x}-\frac{H}{2\mu}\frac{\mathrm{d}p}{\mathrm{d}x}y=\frac{1}{2\mu}\frac{\mathrm{d}p}{\mathrm{d}x}\left(y^2-Hy\right) \tag{11}$$

where H is the height of the channel. To integrate the above equation along y direction of the channel, the average velocity can be obtained. Therefore, the mass flow rate (Q_{m}) in the channel can be found as follows:

$$Q_{\mathrm{m}}=-\frac{H^3 w\rho}{12\mu}\frac{\mathrm{d}p}{\mathrm{d}x}=-\frac{H^3 w p^{\frac{1}{k}}}{12\mu p_{\mathrm{o}}^{\frac{1}{k}}\rho_{\mathrm{o}}^{-1}}\frac{\mathrm{d}p}{\mathrm{d}x} \tag{12}$$

where w is the width of the channel and the subscript o refers to the condition at the outlet of the channel. The above equation can be re-arranged as follows:

$$Q_{\mathrm{m}}\mathrm{d}x=-\frac{H^3 w p^{\frac{1}{k}}}{12\mu p_{\mathrm{o}}^{\frac{1}{k}}\rho_{\mathrm{o}}^{-1}}\mathrm{d}p \tag{13}$$

One can integrate above equation from the entrance to any location, x, in the channel and obtain the pressures distribution inside the channel as follows:

$$p_x=\left(p_{\mathrm{i}}^{\frac{k+1}{k}}-\frac{12Q_{\mathrm{m}}x\left(\frac{k}{k+1}\right)\mu p_{\mathrm{o}}^{\frac{1}{k}}\rho_{\mathrm{o}}^{-1}}{H^3 w}\right)^{\frac{k}{k+1}} \tag{14}$$

where the subscript i refers to the condition at the inlet. For the case when the heat transfer occurs (with a given heat flux boundary condition on the wall), the wall is no longer adiabatic. The above equation can be modified with k replaced by n and is written as follows:

$$p_x=\left(p_{\mathrm{i}}^{\frac{n+1}{n}}-\frac{12Q_{\mathrm{m}}x\left(\frac{n}{n+1}\right)\mu p_{\mathrm{o}}^{\frac{1}{n}}\rho_{\mathrm{o}}^{-1}}{H^3 w}\right)^{\frac{n}{n+1}} \tag{15}$$

where n can be obtained by fitting the above equation to the pressure distribution data. In this way, the pressure variation with either the density or the temperature can be found by a polytropic process as follows:

$$\frac{p}{\rho^n}=\text{const.} \tag{16}$$

3 Device fabrication

3.1 Design consideration

The channel has the inside dimensions of 37 μm in height, 500 μm in width, and 4000 μm in length, with a total of 11 pressure sensors arranged along the both sides of the channel, as shown in Fig. 1. A detailed design of the 3-D structure of current micro-sensor arrays together with a micro-channel system is shown in Fig. 5. In order to allow for deformation of diaphragm, a cavity beneath the diaphragm is made, which is enclosed and sealed by a

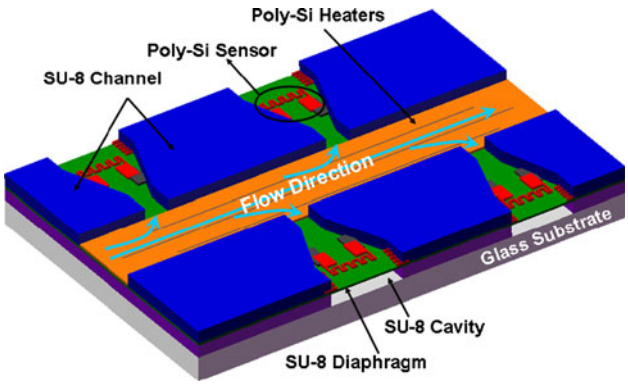

Fig. 5 The 3-D structure of micro-flow channel system including arrays of pressure sensors and the micro-channel

substrate. The sealed cavity allows the diaphragm to recover back to the original position when the channel has no pressure force. In this way, the diaphragm is not used as the top wall of the channel. The deformation of diaphragm will not cause deformation of the entire channel and affect the flow and transport process inside the channel.

The bottom wall of the channel wall is integrated with two sets of micro-heaters, in addition to the temperature sensor arrays that can be heated uniformly. All the other side walls can be made with the low thermal conductivity materials (e.g., polymer) that can provide good insulation. The temperature sensor designed has 5 μm in width and 500 μm in length. The gap width between the neighboring temperature sensors is 200 μm. Either the sensor or the heater layer deposited has 0.2 μm in thickness. The heater strips are distributed uniformly along the entire bottom wall of the channel.

Polysilicon doped with different concentrations of boron is used and fabricated as miniaturized temperature, pressure sensors, or micro-heaters, respectively. Among them, temperature sensors require a large resistance variation with temperature to measure the temperature distribution in the micro-channel. However, both the pressure sensors and the heater are not allowed to have any resistance variation with the temperature in order that the pressure measurements are not affected by the temperature variation inside the channel, while the heaters can provide a constant heat flux without affected by the temperature variation on the wall. Therefore, a higher concentration of the dopants is used in both the pressure sensor and the heaters, and a lower concentration of the dopants is used in the temperature sensors. Therefore, both the heater and the pressure sensors are heavily doped with boron at concentration of 10^{20} atoms/cm^3, the resistivity is almost independent of temperature. For the temperature sensors doped with boron at concentration of 10^{19} atoms/cm^3, the resistivity varies indeed very linearly with temperature. During the heat transfer experiments, measurements of sensor resistivity are made which can be used to find the temperature. The sensitivity of the silicon-doped sensor is relatively high as compared with the metal or the thermocouple sensors. Validation and discussion for these sensors and heaters can be found in the report (Ko 2009). These micro-sensors and the heaters are fabricated and doped initially on a silicon substrate, which is a high-temperature process. These sensors and heaters are then moved to a glass substrate by bonding with the glass substrate and removing the silicon substrate by wet etch. The micro-channel is then fabricated on the glass substrate containing the micro-sensors and the heaters by spin coating and photolithography of the SU-8 materials, which is a low temperature process. The clear separation of the high-temperature fabrication process for the micro-sensors and the heaters with the low-temperature fabrication process for the channel and the diaphragm makes fabrication of the complex channel system possible. After completion of the channel, a constant heat flux can be provided by the heaters and is used as a thermal boundary condition of the current channel.

3.2 Fabrication process

Detailed fabrication process for this complex channel system is described in the following:

1. A 0.1-μm thick LPCVD nitride is deposited on the Si (100) wafer and used as protection mask.
2. The temperature sensors were made by deposition of 0.3-μm thick LPCVD polysilicon film which is then implanted by boron with dose of 3×10^{14} atoms/cm^2. After annealing at 950°C for 30 min, doped film is patterned as temperature sensors, as shown in Fig. 6a.
3. After deposition of 0.3-μm thick LPCVD TEOS as insulation, an 0.3-μm thick LPCVD polysilicon layer is deposited and implanted heavily with boron at concentration of 3×10^{15} atoms/cm^2. After annealing at 950°C for 30 min, the doped polysilicon is patterned as both the heaters and the arrays of pressure sensors.
4. A 0.3-μm thick LPCVD TEOS layer is deposited again as insulation with contact holes opening for metallization. The Cr/Au metal was deposited by E-Beam with a thickness of 0.03/0.3 μm, respectively, and patterned into circuits, as shown in Fig. 6b.
5. A 9-μm thick SU-8 layer is spin-coated on the substrate as the pressure sensing diaphragm. Then, a 50-μm thick SU-8 layer is spin-coated again on the substrate and patterned into the arrays of active cavities to allow for movement of the pressure diaphragm. It is noted that there is a soft bake before light exposure to evaporate the solvent and a post-exposure bake to make the edge between the exposed and the unexposed region more sharp and clear. Finally, instead of using the hard bake, a high intensity of

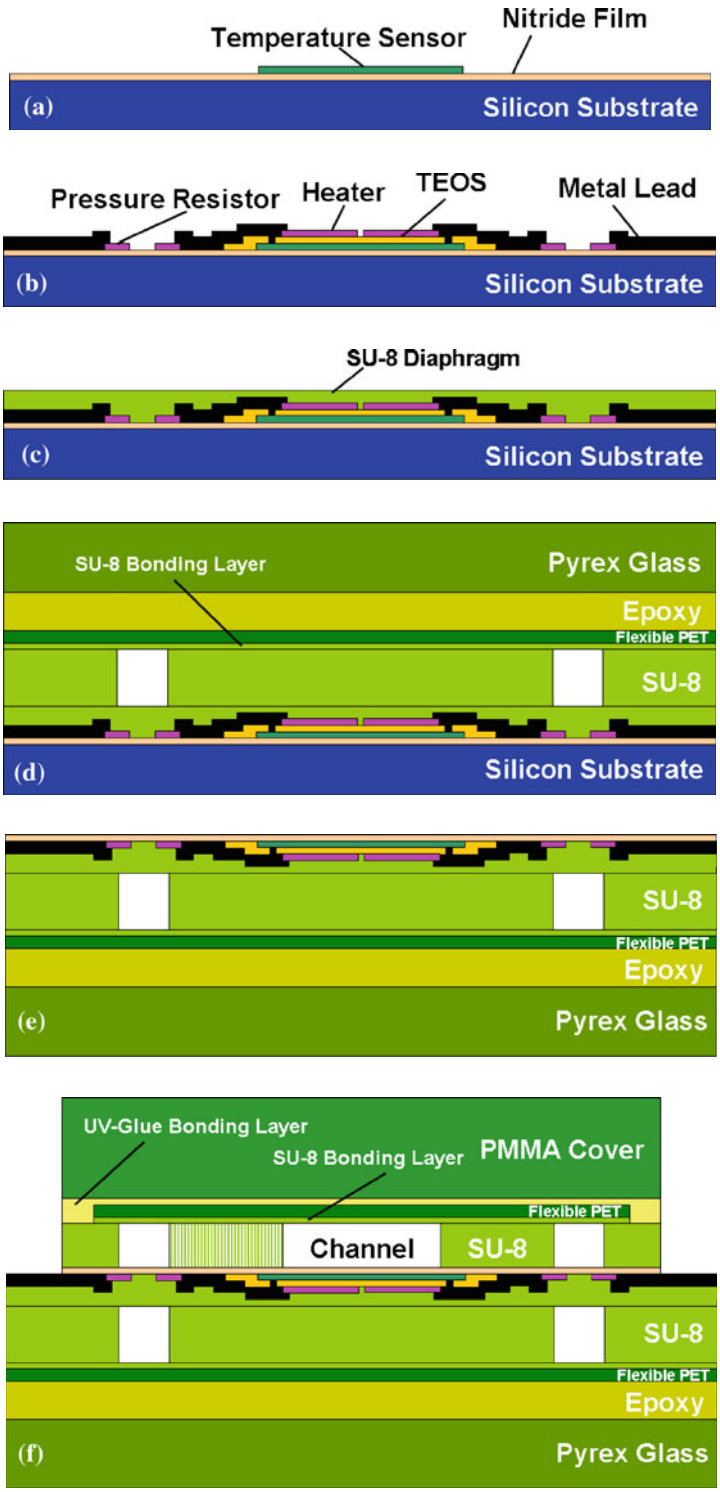

Fig. 6 Fabrication processes of a complicated channel system integrated with miniaturized pressure, miniaturized temperature sensors, and heaters. **a** Deposition of a 0.1-μm thick LPCVD nitride is followed by deposition of a 0.3-μm thick LPCVD polysilicon layer which is patterned into temperature sensors; **b** after deposition of a 0.3-μm thick LPCVD TEOS layer as insulation, a 0.3-μm thick LPCVD polysilicon layer is deposited and patterned into heater and pressure sensors, a 0.3-μm thick LPCVD TEOS layer is deposited as insulation with contact holes opening for metallization; **c** a desired thickness of SU-8 layer is spin-coated on the substrate as a pressure diaphragm; **d** a 50-μm thick SU-8 layer is spin-coated and made into the cavities which are enclosed by a flexible PET plate, and then bonded with Pyrex glass with epoxy resin; **e** remove the silicon substrate to move the sensor devices onto Pyrex glass substrate; **f** another SU-8 layer is spin-coated on the epoxy-glass substrate at desired thickness and patterned as a rectangular micro-channel, after a flexible PET plate is used to enclose the channel, a PMMA plate is then bonded

light is used to illuminate to complete the cross-linking of the resin since the hard bake requires a temperature at 200°C that can damage the underneath thick epoxy layer (refers to the epoxy layer mentioned in item 5 below). For the soft bake, the SU-8 layer is first maintained at 65°C for 7 min with a 5°C/min ramping rate starting from room temperature, and then baked at 95°C for 15 min with a 5°C/min ramping rate starting from 65°C to release the internal residual stress of the SU-8 thick layer. In fact, the success of the SU-8 channel strongly depends on the baking process after light exposure.

6. It is now ready to move the devices made on the Si wafer onto a low thermal conductivity Pyrex glass. This can provide a better insulation for the heaters

which can provide a uniform heat flux boundary condition on the wall. This is done first by bonding the silicon wafer with the Pyrex glass, as shown in Fig. 6b, using epoxy resin as the bonding agent. Since the epoxy resin has a significantly lower thermal conductivity than the Pyrex glass, this can better reduce the heat loss from the channel to the ambient.

7. After the bonding process, the silicon substrate is ready for removal and cleared off. This is done by wet etch the silicon with TMAH solution at 90°C for 5–6 h. Instead of using KOH, the selection of TMAH is attributed to its relatively high selectivity for silicon versus oxide. This can avoid the sensors attacked by the etchant during the long period of wet etch process since the protection layer of the sensors are made of TEOS oxide. After successful movement of the pressure sensors onto the Pyrex glass substrate, no distortion was found.
8. cNext, another SU-8 layer is spin-coated on the epoxy-glass substrate at desired thickness and patterned by lithography to form a rectangular micro-channel and arrays of cavities for the pressure sensors that connect with channel through narrow size tunnels, as shown in Fig. 7a. The side walls of the channel, the narrow tunnels, or the cavities of the pressure sensors are successfully made, as shown in Fig. 7a. It is noted that a similar post-exposure bake should be made to obtain a nice shape of channel and cavities of the pressure sensor arrays.
9. In order to ensure good bonding of the channel and the surrounding cavities, a PET thin plate pre-coated with the SU-8 is used to enclose the channel and cavities. Then a PMMA plate is bonded, using epoxy resin, with the epoxy-glass substrate to re-enforce the channel, as shown in Fig. 6c.

The completed channel, as shown in Fig. 7b, is ready for pressure drop and heat transfer measurements after connecting with air supply system.

4 Experimental apparatus

Before studying the flow characteristics in a micro-channel, the sensor arrays along the channel system were first calibrated by a high precision gas flow supply system. The testing and experimental apparatus are designed and prepared as shown in Fig. 8. For the pressure sensors calibration, air is supplied by a high-pressure source tank that can provide a very steady air flow for at least 10 h. Air is first filtered to remove particles, stored in a tank to stabilize the flow, and then controlled by a close loop pressure controller (TESCOM ER 3000) to keep at desired pressure or pressure cycles by feedback signal from commercial pressure transmitter (TESCOM 615 Series, calibrated by the TESCOM

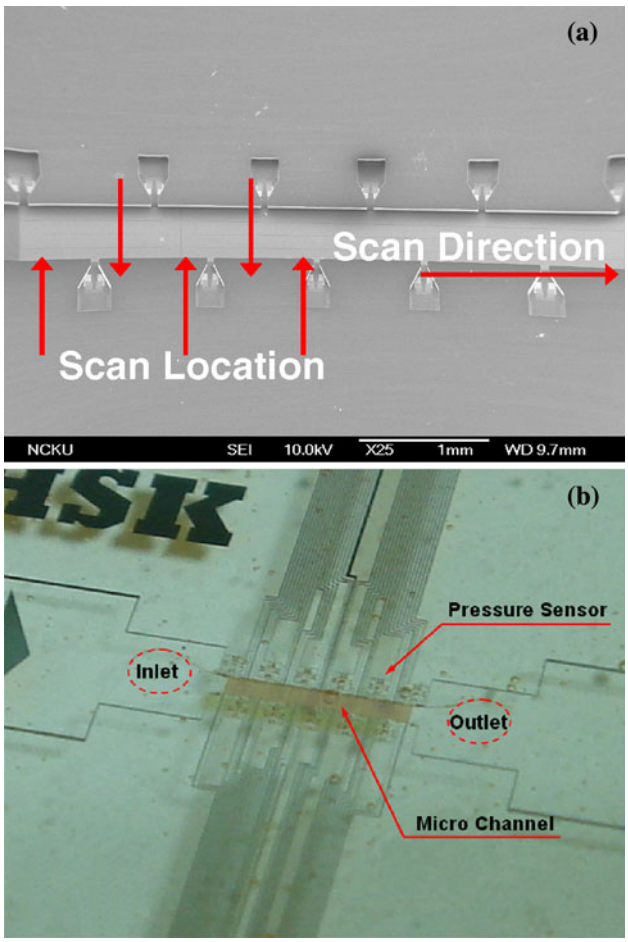

Fig. 7 **a** The SEM picture for SU-8 channel with arrays of pressure sensors and **b** picture for the completed micro-flow channel system

Co., with accuracy about 0.1% for range 0–413 kPa). The signals of sensors inside the micro-channel are wire bonded and connected to a FLUKE-2645A data-logger, which is linked to a personal computer for data processing and plotting. In the flow characteristic study, the pressure controller is replaced by a mass flow controller (Brooks 5858E, calibrated by the Brooks Co., with measurement accuracy of 3% for 1–1000 sccm) to provide accurate mass flow rate that can be read out from a meter display, as shown in Fig. 8. The average airflow velocity at the inlet of the channel can be readily calculated from the mass flow rate, the cross-section area at the inlet of the channel, and the density at the temperature of the flow at the inlet.

5 Results and discussion

5.1 Pressure drop

Typical results of the pressure distributions for the case without heat transfer and their comparison with the

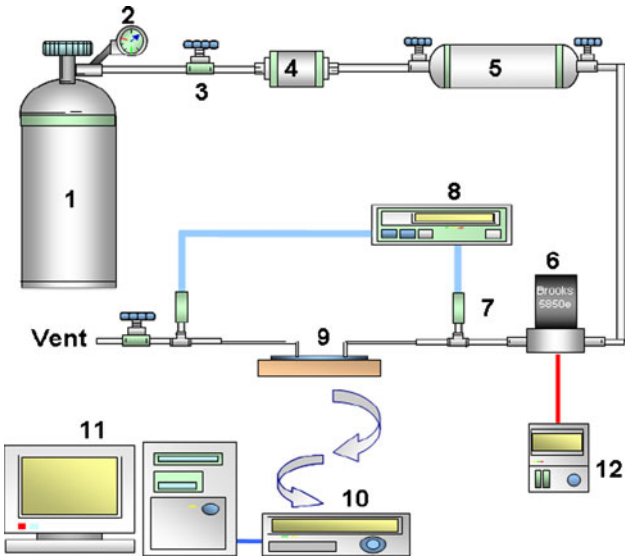

Fig. 8 Gas supply system for heat transfer and pressure drop measurements in micro-channel (*1*) gas tank, (*2*) pressure gauge, (*3*) regulator, (*4*) gas filter, (*5*) gas storage tank, (*6*) mass flow controller (Brooks 5850E), (*7*) pressure and temperature transmitter, (*8*) AD824 translator, (*9*) micro-channel system, (*10*) data acquisition, (*11*) personal computer, (*12*) control panel for mass flow controller

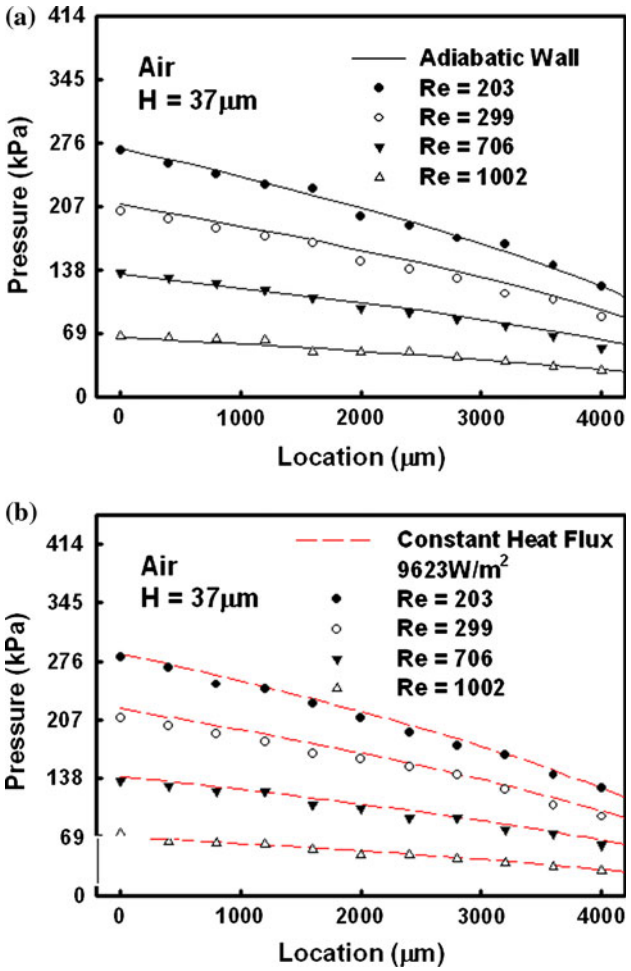

Fig. 9 **a** Comparisons of the pressure distributions between the current data and the analytical results for the airflow along the micro-channel for the case of adiabatic wall and **b** under constant wall heat flux, Eq. 15 is used to fit the data by varying the value of *n*

prediction is shown in Fig. 9a. The agreement between the data and the prediction is very good. There is no any reduction or enhancement in the friction on the wall, which might be due to either reduction in the viscosity or the surface roughness effect. Both the data and the prediction indicate that the pressure distribution inside is not linear, due to the compressibility effect of the air flow, except when the flow rate in the channel become very low and the air flow can be assumed as incompressible. The agreement between the data and the prediction is very good even in the upstream region close to the entrance. Therefore, this means that the pressure distribution in the region close to the entrance has reached a fully developed flow. This clearly indicates that the hydrodynamic entry length in the micro-channel flow is very short as mentioned previously in the derivation of the pressure distribution equation. Therefore, the assumptions used in the analysis are thus confirmed. In addition, all the pressure data decreases smoothly from the entrance to the exit. There is no any sudden change in the pressure gradient where flow may undergo an earlier onset of transition from laminar to turbulent flow as mentioned by others (Peng and Peterson 1996; Peng et al. 1994), which causes greater skin friction coefficient in micro-channel.

With the constant heat flux imposed on the wall, the pressure distribution is also measured as shown in Fig. 9b. The pressure variation along the channel is very similar to the case when the channel wall is insulated except that the magnitude of the pressure is higher. Equation 15 is used to fit the pressure distribution data by varying the value of *n* in this equation. The value of *n* determined from the fit can be used to find the relationship between the pressure and the density in the micro-channel under the constant heat flux condition. This pressure versus density relationship is required for determination of the heat transfer coefficient as described in the next section.

5.2 Local heat transfer

The heat transfer experiments are performed when the heaters inside the channel are turned on. The velocity of the air flow is controlled and is in the laminar flow regime where the *Re* varies from 203 to 1006. The heat transfer coefficient, h_b, can be determined from the following equation:

$$h_b = \frac{\dot{q}_w}{(T_w - T_b)} \tag{17}$$

where $\dot{q}_w$ is the heat flux imposed along the wall by the electric heaters, and is equal to the product of the voltage and the current passing through the heater divided by the total area of the heater. T_w is the wall temperatures measured by the temperature sensors along the channel at a particular location x. T_b is the bulk temperature of the flow which can be estimated from the amount of heat flux imposed on the wall which heats up the air flow and rises up the temperature. By applying conservation of energy over a control volume for the flow in the channel as discussed by Incropera et al. (2007), one can obtain a conservation equation of energy as follows:

$$\dot{q}_w \pi D_h dx = \dot{m} c_p dT_b \tag{18}$$

where $\dot{m}$ is the mass flow rate of the air in the channel. Rearranging and integrating the above equation from the inlet of the channel, one can obtain:

$$\int_{T_i}^{T_b} dT_b = \int_0^x \frac{\dot{q}_w \pi D_h}{\dot{m} c_p} dx. \tag{19}$$

Therefore,

$$T_b = T_i + \frac{\dot{q}_w \pi D_h}{\dot{m} c_p} x \tag{20}$$

Once the heat transfer coefficient is obtained, the local Nusselt number, Nu_b, can be found from the definition as follows:

$$Nu_b = \frac{h_b \times D_h}{K} \tag{21}$$

where K is the thermal conductivity of the air flow.

The thermal conductivity of the air used in the Nusselt number is evaluated at the mean bulk temperature, i.e., an average of the bulk temperature of the flow at the inlet and the outlet of the channel. The Nusselt number results obtained for the cases of the heat flux varied from 5413 to 21652 W/m^2 with the Reynolds number at 500 are compared with the prediction for the parallel plate channel (Rohsenow et al. 1985), as shown in Fig. 10a. The Nusselt number results in the micro-channel is significantly higher than the prediction for a large-scale parallel plate channel (Rohsenow et al. 1985), and become closer as the heat flux on the wall decreases. For the case of heat flux equal or lower than 9623 W/m^2, all the Nusselt number results collapse into a single line, as shown in Fig. 10b, in the downstream of the channel where flow has become thermal fully developed. The Nusselt number results collapsing into a single curve in the fully developed region agrees with the prediction for large-scale channel except that the Nusselt number is higher. This indicates that other effects, such as property variation with temperature and or compressibility of flow, should be taken into account to obtain a good correlation of the heat transfer data.

The reason for this deviation can be attributed to the property variation, especially the compressibility of the gas flow, which leads to increase in the heat transfer. In order to account for the compressibility of the gas which can expand, reduce the kinetic energy, and change the bulk temperature of the flow, the governing equation for the bulk temperature should be re-derived from concept of energy balance as follows:

$$d\dot{q} = \dot{m}(e_2 - e_1) + \left(\frac{U_2^2}{2} - \frac{U_1^2}{2}\right) \tag{22}$$

where e is enthalpy and the subscript 1, 2 indicates properties at the inlet and the outlet of a control volume,

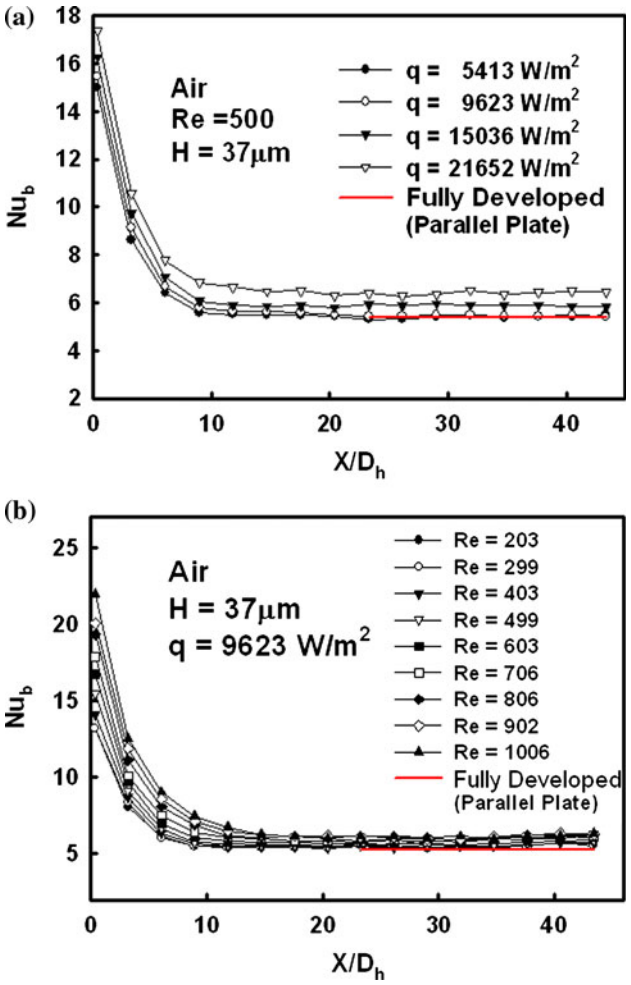

Fig. 10 Experimental results for local Nusselt number distributions under different **a** heat flux conditions and **b** Reynolds numbers

respectively. For a differential control volume, the above equation can be written as

$$\mathrm{d}\dot{q} = \dot{m}\mathrm{d}e + \mathrm{d}\left(\frac{U^2}{2}\right) \tag{23}$$

where $\mathrm{d}q = \dot{q}_\mathrm{w}\pi D_\mathrm{h}$, and $\mathrm{d}e = c_p\mathrm{d}T$, re-arranging the above equation, one obtains

$$\frac{\mathrm{d}T_b}{\mathrm{d}x} = \frac{\dot{q}_\mathrm{w}\pi D_\mathrm{h}}{\dot{m}c_p} - \frac{\mathrm{d}\left(\frac{U^2}{2}\right)}{c_p\mathrm{d}x}. \tag{24}$$

To integrate above equation from the entrance to a desired location, x, downstream in the channel, one can obtain the bulk temperature of the flow as follows:

$$T_\mathrm{b} = T_\mathrm{i} + \frac{\dot{q}_\mathrm{w}\pi D_\mathrm{h}}{\dot{m}c_p}x - \left(\frac{U_x^2}{2} - \frac{U_\mathrm{i}^2}{2}\right)\frac{1}{c_p} \tag{25}$$

From the continuity equation,

$$\rho_1 A_1 U_1 = \rho_2 A_2 U_2 \tag{26}$$

The bulk temperature can be re-arranged as follows

$$T_\mathrm{b} = T_\mathrm{i} + \frac{\dot{q}_\mathrm{w}\pi D_\mathrm{h}}{\dot{m}c_p}x - \frac{U_\mathrm{i}^2}{2c_p}\left[\left(\frac{\rho_\mathrm{i}}{\rho_x}\right)^2 - 1\right]. \tag{27}$$

Since the current micro-channel is actually fabricated by very low thermal conductivity materials, the channel wall can be considered as well insulated. Without heat transfer into the channel, the gas flow inside the channel can be assumed to be undergoing isentropic process. For the case when a desired heat flux is imposed on the bottom wall, the gas is assumed under polytropic process and the pressure density relationship can be found from Eq. 16 where n is determined from the heating condition on the wall of the channel by fitting this equation with the pressure distribution data, as discussed previously. Therefore, the density in Eq. 27 can be replaced by the local pressure as follows:

$$T_\mathrm{b} = T_\mathrm{i} + \frac{\dot{q}_\mathrm{w}\pi D_\mathrm{h}}{\dot{m}c_p}x - \frac{U_\mathrm{i}^2}{2c_p}\left[\left(\frac{p_\mathrm{i}}{p_x}\right)^{\frac{2}{n}} - 1\right]. \tag{28}$$

From the local pressures measured by current pressure sensor arrays along the micro-channel, the bulk temperature can be re-calculated from the above equation. Therefore, the local Nusselt numbers along the channel can be obtained, as shown in Fig. 11 for different Reynolds number conditions. All the Nusselt number results collapse into a single curve in the fully developed region, as shown in Fig. 11a for different heat flux conditions. For the case of heat flux at 9623 W/m^2, the Nusselt numbers at different Reynolds numbers also collapse into a single curve in the fully developed region, as shown in Fig. 11b, but the curve is slightly lower than

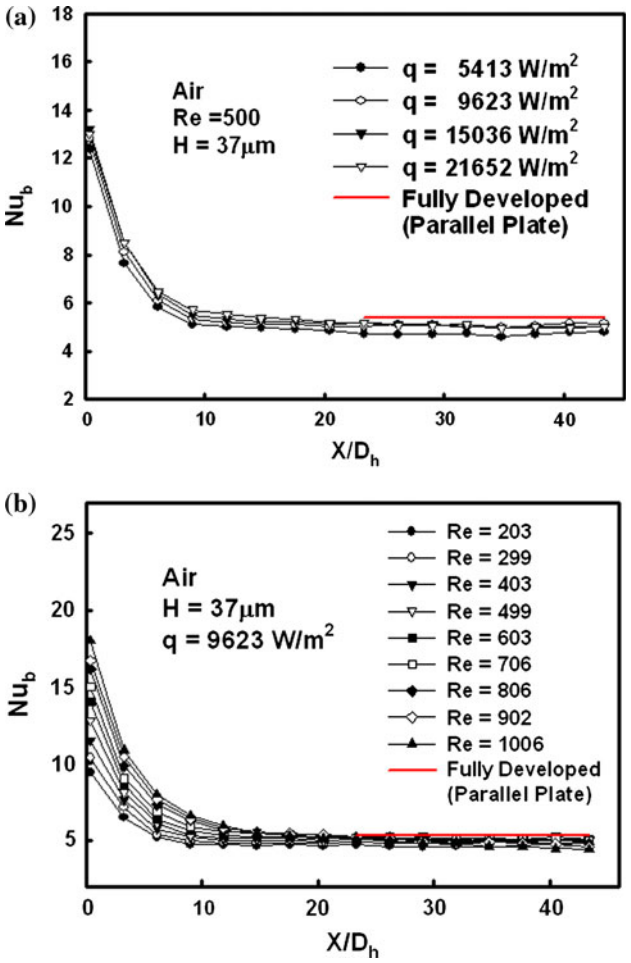

Fig. 11 Re-calculated results for local Nusselt number distributions under different **a** wall heat flux conditions and **b** Reynolds numbers

the prediction for large-scale channel. Theoretical results for the Nusselt numbers in the fully developed region of a large-scale rectangular channel at different aspect ratios can be found in the book (Incropera et al. 2007). It is found that in large-scale channel the Nusselt number is 4.55 for a rectangular channel with aspect ratio of 1:10, but is 5.38 for a parallel plate channel. In fact, the current micro-channel is not a parallel plate channel but is a channel with aspect ratio of 1:13. Therefore, a lower Nusselt number data in the current channel than the prediction for a parallel plate channel is expected and is attributed to the effect of the aspect ratio.

In order to compare the heat transfer in the entrance region, the flow is assumed to be hydrodynamically fully developed before entering into the channel, and the problem becomes a thermal entry length problem because the hydrodynamic entry length is very short as described previously. In the thermal entry length region, the heat transfer process can be correlated in terms of the Graetz number as defined in the following (Incropera et al. 2007):

$$Gz = \frac{Re\,\mathrm{Pr}}{x/D_\mathrm{h}} \tag{29}$$

The thermal entry length in the large-scale tube can be usually expressed as (Incropera et al. 2007),

$$Gz^{-1} \sim 0.05. \tag{30}$$

The entry length shown above is found at the location where the Nusselt number approaches a constant value. From the heat transfer data, as shown in Fig. 12, the entry length in the current micro-channel can be found as,

$$Gz^{-1} \sim 0.023. \tag{31}$$

It appears that the current heat transfer data does not have a similar trend as in a large-scale tube. This is attributed to the fact that the current micro-channel is not a circular tube. A correlation from the numerical results in the entry region of a large-scale parallel plate channel is found by Naito (1984) and can be expressed as follows:

$$Nu_x = 0.461043Gz^{1/2}\Big(1 + 6.35257Gz^{-1/2} - 33.4079Gz^{-1} + 419.158Gz^{-3/2} - 1537.84Gz^{-2}\Big). \tag{32}$$

Comparison of the local Nusselt numbers between the data for the current micro-channel and the correlation from the prediction for a large-scale channel is made, as shown in Fig. 12. The agreement in entrance region is very good except that in the fully develop region the current data is slightly lower due to the aspect ratio effect.

Since most of the heat transfer data reported for micro-channel flow is the average heat transfer coefficient or the average Nusselt number, comparison with these data can be made when the local Nusselt number is averaged as follows:

$$Nu_\mathrm{ave} = \frac{1}{x}\int_0^x Nu_\mathrm{b}\mathrm{d}x \tag{33}$$

The averaged Nusselt numbers in the current micro-channel are first compared, as shown in Fig. 13, with the correlation predicted by Naito for air flow in large-scale parallel plate channel. The average Nusselt number is very close, but smaller than the correlation obtained by Naito (1984). This is attributed to the effect of the aspect ratio of the current channel. The narrow size of the channel in the transverse direction of the flow can reduce the flow motion near both the end walls of the channel which can significantly reduce the heat transfer. The result is of interest to compare current heat transfer data with the results of others in micro- or large-scale channel. To avoid influence of EDL in liquid flow, comparison is limited to the data for air flow in the channels. In general, when $Re > 2300$, the flow inside the channel becomes turbulent. The average Nusselt number for $Re > 2300$ is much larger than for $Re < 2300$ (Rohsenow et al. 1985; Morini 2004). For large-scale channel, the Nusselt number in the parallel plate channel is, in general, greater than that in the circular tube (Incropera et al. 2007). This is indicated in Fig. 14 where the average Nusselt numbers of both the numerical results from Naito (1984) and the experimental data for the current rectangular channel is higher than the correlation for the circular tube (Incropera et al. 2007). The heat transfer correlations obtained by Choi et al. (1991) is for air flow in micro-tubes. Their data is much smaller than the correlation of Hausen (Incropera et al. 2007). The much lower Nusselt number and the significant increase with the Reynolds number in

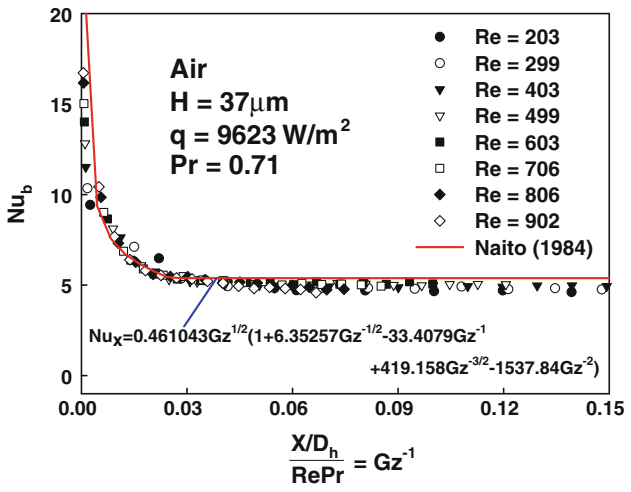

Fig. 12 Comparison of the local Nusselt numbers between correlation from the prediction for large-scale channel and the experimental data

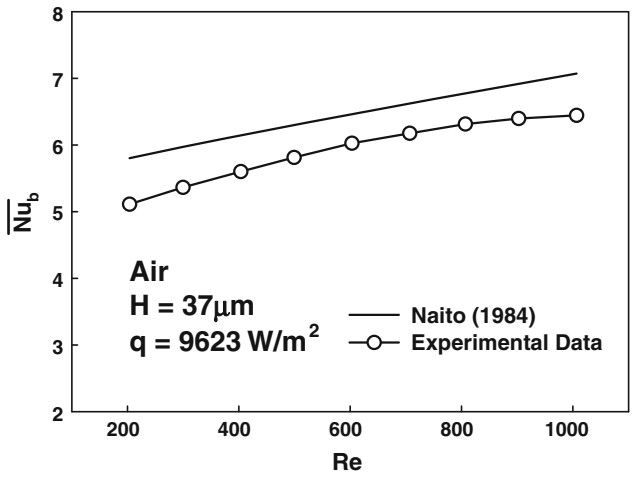

Fig. 13 Comparison of the average Nusselt numbers in the current micro-channel with the correlation predicted by Naito for air flow in large-scale parallel plate channel

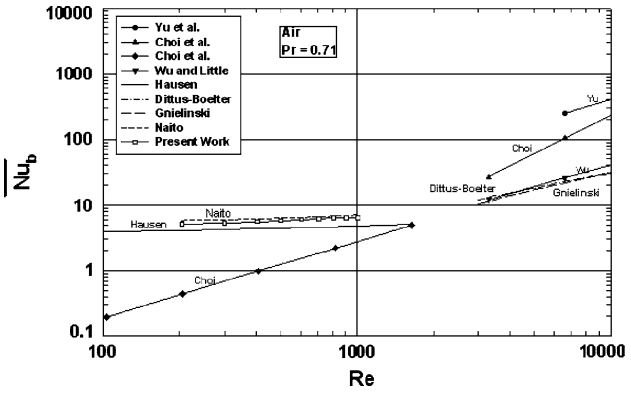

Fig. 14 Comparison of average Nusselt numbers between the current results and published data

Choi's data are attributed to the streamwise conduction of heat along the micro-tube. The micro-tubes used in the past were made of stainless steel which is convenient for electric heating, and is expected to cause large streamwise conduction of heat in the finite thickness of the tube since the thermal conductivity of stainless steel is relatively high and is in the range from 13 to 15 W/mK depending upon the types of the steel used. However, the streamwise conduction of heat along the wall of the current micro-channel has been minimized due to the use of a thick layer of epoxy which has a very low thermal conductivity. In addition, wall roughness in the micro-tubes of Choi is expected to be large enough which may result in the discrepancy. However, the roughness of their micro-tubes is not reported. When going into turbulent flow region, the heat transfer data from different work in micro-channel scatter very much, but are all higher than those in large-scale channel (Morini 2004; Kays et al. 2005; Wu and Cheng 2003; Yu et al. 1995). It is noted that data from the work of both Dittus-Boelter and Gnielinski (Rohsenow et al. 1985) are for air flow in large-scale tubes. The higher heat transfer data in micro-channel can be attributed to wall roughness effect in the micro-tubes. It has been realized (Rohsenow et al. 1985; Kays et al. 2005) that wall roughness can significantly enhance turbulent heat transfer in the large-scale tube. Thus, the wall roughness is expected to significantly enhance turbulent heat transfer in the micro-channel. Unfortunately, the wall roughness on each of the micro-tube wall has not been reported and can be expected to be very high in the micro-stainless steel tubes if no special treatment on the surface is provided.

6 Conclusions

A complicated micro-channel system integrated with arrays of micro-pressure and temperature sensors has been made. The channel made employs polymer materials which make the fabrication process much simpler. The channel can be heated uniformly on the bottom with two sets of micro-heaters so that a uniform wall heat flux boundary condition can be provided. With correct measurement of Young's Modulus for SU-8, the design procedure for the micro-pressure sensor can be much simpler using approximate solution for the maximum deflection and strain of the diaphragm. The channel fabricated allows measurements of both the local temperature on the heated wall and the pressure distribution along the channel. With a simplified analysis for the pressure drop modified for the case when the heat transfer occurs, this allows accounting for the compressibility of the air flow and correct reduction of the local heat transfer data. Both the local and the average Nusselt numbers measured have been compared with prediction for incompressible flow in large-scale channel. The comparison has clarified many of the conflicting results among different works as indicated in Fig. 14.

Acknowledgment This research was sponsored by Council of Taiwan under contact no. NSC 97-2221-E-006-057-MY2.

References

Bayraktar T, Pidugu SB (2006) Review: characterization of liquid flows in microfluidic systems. Int J Heat Mass Transf 49: 815–824

Boresi AP, Schmidt RJ, Sidebottom OM (1993) Advanced mechanics of materials. Wiley, New York, pp 538–539

Choi SB, Barron RF, Warrington RO (1991) Fluid flow and heat transfer in microtubes. ASME DSC 32:123–134

Craighead H (2006) Future lab-on-chip technologies for interrogating individual molecules. Nature 442(27):387–393

Dellmann L, Roth S, Beuret C, Racine G A, Lorenz H, Despont M, Renaud P. Vettiger P (1997) Fabrication process of high aspect ratio elastic structures for piezoelectric motor applications. Transducers 97 Chicago, USA

Dongari N, Sharma A, Durst F (2009) Pressure-driven diffusive gas flows in micro-channels: from the Knudsen to the continuum regimes. Microfluid Nanofluid 6:679–692

Guckel H (1990) Surface micromachined pressure transducer. Sens Actuators A 28:133–146

Guckel H, Christenson TR, Skrobis KJ, Sniegowski JJ, Kang JW, Choi B, Lovell EG (1990) Microstructure sensors. In: IEEE international electron devices meeting, pp 613–616

Incropera FP, DeWitt DP, Bergman TL, Lavine AS (2007) Fundamentals of heat and mass transfer, Chap. 8, 6th edn. Wiley, New York

Jiang L, Wong M, Yitshak Z (1999) Phase change in microchannel heat sinks with integrated temperature sensors. J MEMS 8:358–365

Kays WM, Crawford ME, Weigand B (2005) Convective heat and mass transfer, Chap. 8, 4th edn. McGraw-Hill, New York

Ko HS (2009) Fabrication and development of micro fluidic system with embedded micro pressure and temperature sensors for study of thermal and fluid flow properties. PhD thesis National Cheng Kung University, Tainan, Taiwan

Ko HS, Liu CW, Gau C (2007a) A novel fabrication for pressure sensor with polymer material and evaluation of its performance. J Micromech Microeng 17:1640–1648

Ko HS, Liu CW, Gau C, Yang CS (2007b) Fabrication and design of a heat transfer micro-channel system by a low temperature MEMS technique. J Micromech Microeng 17:983–993

Ko HS, Liu CW, Gau C, Jeng DZ (2008) Flow characteristics in a microchannel system integrated with arrays of micro pressure sensors using polymer material. J Micromech Microeng 18: 075016

Koo J, Kleinstreuer C (2003) Liquid flow in microchannels: experimental observations and computational analyses of microfluidics effects. J Micromech Microeng 13:568–579

Lee WY, Wong M, Zohar Y (2002) Pressure loss in constriction microchannels. J Microelectromech Syst 11(3):236–244

Li D (2004) Electrokinetics in microfluidics, vol 2. Elsevier, Oxford

Lorenz H, Despont M, Fahrni N, LaBianca N, Renaud P, Vettiger P (1997) A low-cost negative resist for MEMS. J Micromech Microeng 7:121–124

Morini GL (2004) Single-phase convective heat transfer in microchannels: a review of experimental results. Int J Therm Sci 43:631–651

Naito E (1984) Laminar heat transfer in the entrance region between parallel plates—the case of uniform heat flux. Heat Transf Jpn Res 13(3):92–106

Natrajan VK, Christensen KT (2010) The impact of surface roughness on flow through a rectangular microchannel from the laminar to turbulent regimes. Microfluid Nanofluid 9:95–121

Peng XF, Peterson GP (1996) Convective heat transfer and flow friction for water flow in microchannel structures. Int J Heat Mass Transfer 39:2599–2608

Peng XF, Peterson GP, Wang BX (1994) Frictional flow characteristics of water flowing through rectangular microchannels. Exp Heat Transf 7:249–264

Prasher RS, Chang J-Y, Sauciuc I, Narasimhan S, Chau D, Chrysler G, Myers A, Prstic S, Hu C (2005) Nano and micro technology-based next generation package-level cooling solution. Intel Technol J 9(4):285–296

Rohsenow WM, Hartnett JP, Ganic EN (1985) Handbook of heat transfer fundamentals, 2nd edn. McGraw-Hill, New York, pp 7–49

Rostami AA, Mujumdar AS, Saniei N (2002) Flow and heat transfer for gas flowing in microchannel: a review. Heat and Mass Transfer 38:359–367

Tuckerman DB, Pease RFW (1981) High-performance heat sinking for VLSI. IEEE Electron Device Lett 2:126–129

Wu HY, Cheng P (2003) Friction factors in smooth trapezoidal silicon microchannels with different aspect ratios. Int J Heat Mass Transf 46:2519–2525

Yu D, Warrington RO, Barron R, Ameel T (1995) An experimental and theoretical investigation of fluid flow and heat transfer in microtubes. In: Proceedings of ASME/JSME thermal engineering joint conference, Maui, pp 523–530

Zohar Y, Lee YK, Lee WY, Jiang L, Tong P (2002) Subsonic gas flow in a straight and uniform microchannel. J Fluid Mech 472: 125–151